sustainability

MDPI

Article

Deep Insights into the Radiation Shielding Features of Heavy Minerals in Their Native Status: Implications for Their Physical, Mineralogical, Geochemical, and Morphological Properties

Mostafa A. Masoud [1,*], Ahmed M. El-Khayatt [2,*], Mohammad W. Marashdeh [2], Mohamed G. Shahien [1], Bottros R. Bakhit [3], Wael Abdelwahab [4], Mohamed Abdel Rafea [2] and Ahmed M. Zayed [1]

[1] Applied Mineralogy and Water Research Lab (AMWRL), Geology Department, Faculty of Science, Beni-Suef University, Beni Suef 62521, Egypt
[2] Department of Physics, College of Science, Imam Mohammad Ibn Saud Islamic University (IMSIU), Riyadh 11642, Saudi Arabia
[3] Geology Department, Faculty of Science, Beni-Suef University, Beni Suef 62521, Egypt
[4] Geological Sciences Department, National Research Centre, El-Buhouth St., Dokki, Cairo 12622, Egypt
* Correspondence: mostafa_masoud@science.bsu.edu.eg (M.A.M.); amelkhayatt@imamu.edu.sa (A.M.E.-K.)

Abstract: Barite and hematite are the most common heavy-weight minerals applied as aggregates in radiation shielding concrete (RSC). Therefore, to limit the cement consumption and reduce the CO_2 emissions accompanying its production, the aim of this study is to use Egyptian barite and hematite minerals in their native status and evaluate their attenuation efficiency against fast neutrons and γ-rays. This was implemented through the measurement of their radiation attenuation against fast neutrons and γ-rays in the energy ranges of 0.80–11 and 0.40–8.30 MeV, respectively, employing a Pu-Be source and a stilbene scintillator. Theoretical calculations were prepared using the NXcom program to validate the fast neutron attenuation measurements. Furthermore, the implications of the physical, mineralogical, geochemical, and morphological characteristics of these heavy-weight minerals with respect to their attenuation efficiencies were considered. We found that barite has superior radiation attenuation efficiency for fast neutrons and γ-rays compared to hematite by 9.17 and 51% for fast neutrons and γ-rays, respectively. This was ascribed to the superior physical, mineralogical, geochemical, and morphological properties of the former relative to those of the latter. Furthermore, a satisfactory agreement between the experimental and theoretical results was achieved, with a deviation of 16 and 19.25% for the barite and hematite samples, respectively. Eventually, barite and hematite can be successful candidates for their use as sustainable alternatives to common RSC.

Keywords: barite; hematite; radiation attenuation; fast neutrons; gamma rays; NXcom

Citation: Masoud, M.A.; El-Khayatt, A.M.; Marashdeh, M.W.; Shahien, M.G.; Bakhit, B.R.; Abdelwahab, W.; Abdel Rafea, M.; Zayed, A.M. Deep Insights into the Radiation Shielding Features of Heavy Minerals in Their Native Status: Implications for Their Physical, Mineralogical, Geochemical, and Morphological Properties. *Sustainability* **2022**, *14*, 16225. https://doi.org/10.3390/su142316225

Academic Editor: Jonathan Oti

Received: 21 October 2022
Accepted: 30 November 2022
Published: 5 December 2022

1. Introduction

In light of the growing concerns about the development of electricity-generating technologies free of CO_2 footprints and other greenhouse gas emissions, many countries have resorted to nuclear reactor technology [1]. This technology has the potential for extensive and clean energy production. However, this type of technology is associated with a dilemma in terms of the hazardous radiation leakage from the nuclear reactors. Applied mineralogy is one of the essential branches of geology which investigates the use of minerals in radiation attenuation applications. One of these applications is the use of minerals as barriers to attenuate the radiation or restrain the radioactive waste resulting from nuclear reactors or radiotherapy centers [2,3]. Such radioactive waste is associated with the dual problems of disposal and health hazards due to the release of ionizing radiation, including neutrons, and γ-rays [4]. Such radiation can cause genetic damage, developmental irregularities, malignancies, and decreased fertility and fitness [5]. In recent decades, nuclear physicists, engineers, and geologists have developed many

minerals and rock-forming materials to attenuate such radiation. These materials are widely used as aggregates or as additives incorporated into concrete, mortar, glass, and polymers [6–23]. Although concrete is the most prevalent material used to mitigate natural disasters [24] and man-made radiation leakages, a recent trend has occurred with respect to the exploitation of such minerals as native materials (in their original state, without their embedding as aggregates or additives in concrete, composites, or polymers), replacing concrete and cement pastes [25]. The most common types of these natural materials are serpentine minerals [26], halloysite [27,28], barite [29,30], chambersite [31], magnetite, limonite, hematite [30], granite [32,33], serpentinite rocks [34], garnet [35], and quartz [36]. The purposes of this trend are to (1) decrease the pollution resulting from the use of cement as a result of the use of concrete, (2) reduce the energy and costs stemming from the cement industry, (3) exploit the massive reserves of these minerals, which have no benefit to be used as nuclear waste landfills, (4) exploit additional space using thinner shielding walls, and (5) reduce the amount of maintenance that is needed compared to that which is needed for concrete. In particular, barite and hematite are the most effective and widely employed materials for radiation attenuation [17,37,38], owing to their high density, which qualifies them to be the best types of γ-ray−shielding materials. Additionally, they can effectively attenuate fast neutrons by moderation through inelastic collisions of fast neutrons with the heavy nuclei of barium (Ba) and iron (Fe) in barite and hematite, respectively [38,39]. Akkurt et al. [29] experimentally measured the γ-attenuation of barite using ^{137}Cs and ^{60}Co at 0.662 and 1.330 MeV, respectively. They found that there was an agreement between these experimental results when they were correlated with the calculated results obtained by XCOM [29]. Moreover, Oto et al. [30] measured different γ-ray shielding parameters of barite and hematite minerals at 0.081, 0.276, 0.302, 0.356, and 0.383 MeV photons emitted from ^{133}Ba and 0.121, 0.244, 0.344, 0.444, and 0.778 MeV photons emitted from ^{152}Eu using an HPGe detector. They found that the barite and hematite minerals effectively attenuated the γ-rays with a superior competence for the former ones. To the best of our knowledge, the earlier studies [29,30] are the only ones focused on the ability of barite and hematite minerals in their native state to achieve γ-ray attenuation only. However, there are no reports on the effect of the geological features (e.g., mineralogical and geochemical compositions), on the radiation shielding properties of these minerals (i.e., barite and hematite), or on their radiation attenuation ability. Furthermore, their attenuation against fast neutrons has not been discussed to date.

The Baharia Oases were mined for barite and hematite minerals formed as a result of hydrothermal solutions during the Middle Eocene [40]. The reserves of the two minerals have not been recently exploited in the Baharia Oases; however, the quantity of iron ore, the main hematite, amounted to about 270 million metric tons [41]. Therefore, the hematite of the Baharia Oases was the primary feedstock of steel production by the Egyptian Iron and Steel Company (EISC) in Helwan. Nevertheless, the processes of prospecting and mining hematite were stopped, and millions of tons of hematite ore were no longer exploited, particularly after the governmental decision to liquidate EISC in January 2021 due to the costly maintenance and operation processes. Therefore, these reserves of minerals can be harnessed as a permanent underground repository for radioactive waste or as tiles to line the walls of radiotherapy facilities or nuclear reactors. Hence, this study is dedicated to investigating the attenuation properties of hematite and barite in the Baharia Oases in the Western Desert, Egypt, against γ-rays and fast neutrons, focusing on the role of their physical, mineralogical, geochemical, and morphological properties. To this end, we investigated: (1) their physical properties by density and water absorption tests; (2) their mineralogy using X-ray diffraction (XRD), transmitted-light microscopy (TLM), and reflected-light microscopy (RLM); (3) their geochemistry by X-ray fluorescence (XRF); (4) their morphology by scanning electron microscopy (SEM); (5) their radiation attenuation measurements employing a Pu-Be source and a stilbene detector; (6) the theoretical calculations of fast neutron attenuation using NXcom; (7) a comparison of the addressed

samples with the previously studied concrete mixes, which have the same conditions of radiation attenuation measurement.

2. Geologic Description of Materials

2.1. Lithology and Stratigraphy

Many previous studies investigated the geological aspects of the iron ores and barite mineralization in detail, including their lithology, outcrops, and stratigraphy [40,42–48].

Generally, the Baharia Oasis is a large depression in the Western Desert of Egypt. It is located about 270 km southwest of Cairo and 180 km west of the Nile Valley. The outcrop succession of the area is subdivided from the bottom to the top into the lower Cenomanian Baharia Formation, the upper Cenomanian El Heiz Formation, the Campanian El Hufuf Formation, and the Maastrichtian Khoman Chalk Formation. The upper Cretaceous formations are unconformably overlain by the Eocene Naqb, Qazzun, and El Hamra formations. The iron ore deposits are located in the northern part, and they extend over 11.70 km^2 with a thickness ranging from 2–35 m. In that area, the iron ore is restricted to the lower portion of the Middle Eocene limestone of the Naqb Formation. The Naqb Formation consists of hard yellow-brown limestone that is intercalated with marl. As shown in Figure 1, the iron ores are concentrated in three regions, including the Ghorabi, El Harra, and El Gedida [42,49]. The current study focuses on the iron ore of El Gedida due to its high grade and amount of reserves. El Gedida mine is situated within the Naqb Formation hills. The central part of the depression is characterized by a high relief surrounded by the low Wadi area, which comprises the Cenomanian sandstone and clayey sandstone of the Baharia Formation at the base, which is overstepped by the main Lutetian iron ore successions of the Naqb-Qazzun Sequence. The Eocene ironstones are unconformably overlain by the upper Eocene glauconitic clay beds [48]. In the Eastern and Western Wadi areas of the depression, the iron ores are truncated unconformably by Late Eocene (Lutetian–Bartonian) glauconite with lateritic iron ore interbeds of the Hamra Formation [50]. El Aref et al. [50] found that this iron ore sequence is composed of a pisolitic-oolitic ironstone unit which is followed by bedded iron ores intercalated with ferruginous mudstones (Figure 2a). As reported previously by Baioumy et al. [49], the iron ore of the Baharia Oases is mainly composed of hematite and goethite ores.

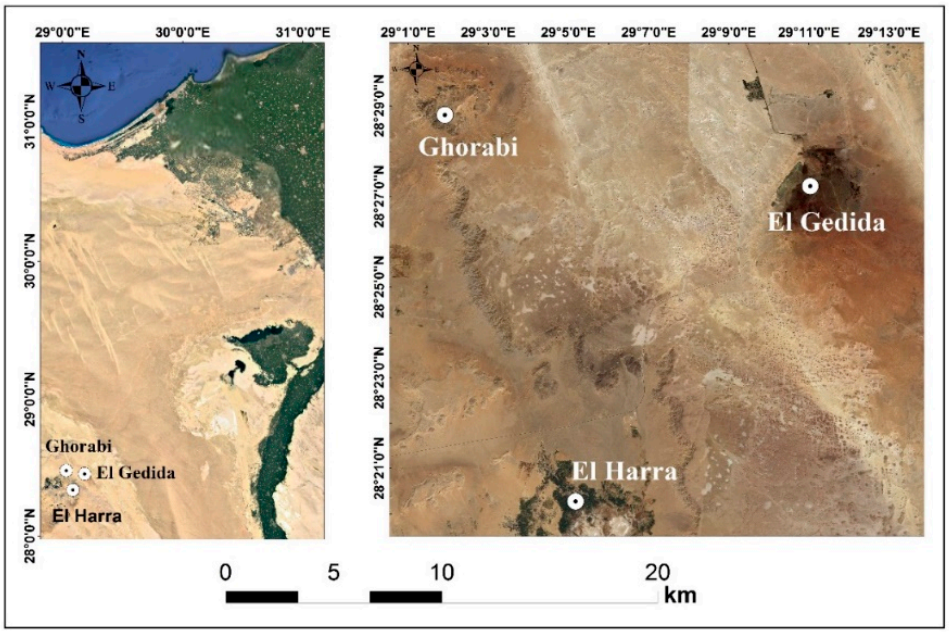

Figure 1. Google satellite map of the collected barite from the Ghorabi mine and hematite from the El Gedida mine.

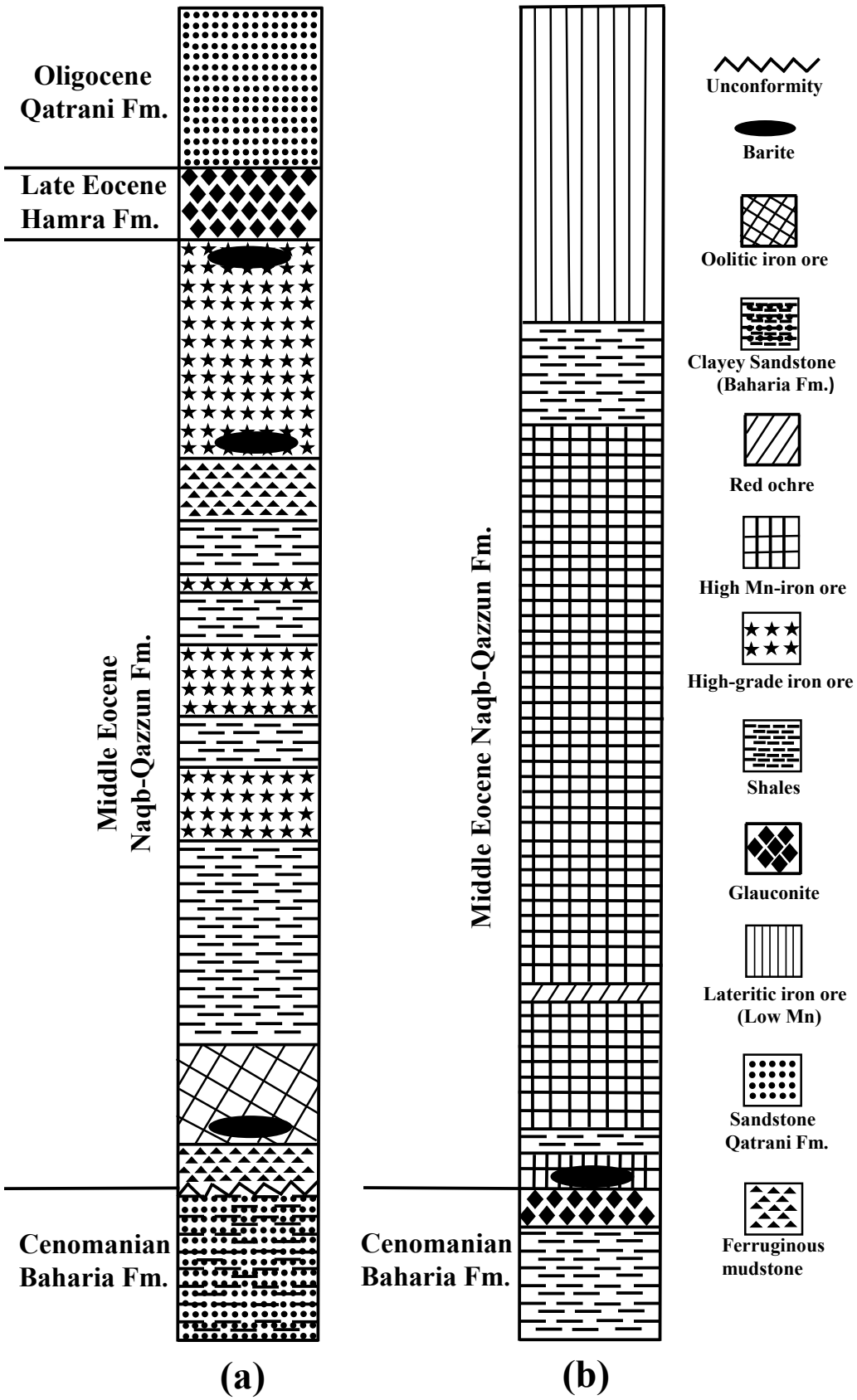

Figure 2. Stratigraphic sections showing the lithology of the iron ores with positions of barite mineralizations along: (**a**) the Eastern Wadi of El Gedida mine area and (**b**) the Ghorabi mine area.

On the other hand, the investigated barite samples were collected from the Ghorabi area, which is characterized by several small, rounded hills that reach 15 m in the large hills and 6 m in the small ones. Barite was recorded as a predominant mineral in the Ghorabi area [47]. In the Ghorabi iron ore deposits, the barite was found at the bottom of the iron deposits, which was mixed in some parts with the iron ore bed. It is supposed that the hydrothermal fluids are responsible for depositing the barite [47]. Baioumy et al. [49] found that the barite was formed in many stratigraphic levels of the ironstone sequences in the shape of stratabound to stratiform barite and as rosettes at the contact between the underlying Baharia Formation and the Middle Eocene ironstone sequences (Figure 2b). Stratiform barite nodules are hosted in the organic-rich green mudstone facies at the bottom of the upper ironstone sequence of the Gabal Ghorabi mine area [51]. As in the El Gedida mine, the main barite deposits are the stratabound karst-related deposits in the Ghorabi mine. They form cavities and fractures, filling the barite pockets and masses. It was found that the secondary enrichment during dissolution and reprecipitation within solution cavities and fractures is responsible for the formation of the stratabound karst-related barite deposits.

2.2. Megascopic Characterization

Field geology is one of the most fundamental means by which geologists can discriminate between various minerals and rocks. This type of characterization requires experience-based knowledge. In this study, by the visual inspection aided by a hand lens, the samples were identified at first sight through their colors, weathering, or physical properties [52].

During the field inspection, barite was detected by its pale brown-yellow color with a glassy luster and a heavy specific gravity (Figure 3a). On the other hand, hematite has different varieties of red colors, including scarlet or dark red, with an earthy feel and a heavy specific gravity (Figure 3b). Besides its earthy luster, the hematite sample has the distinguishing property of its color sticking to the hand.

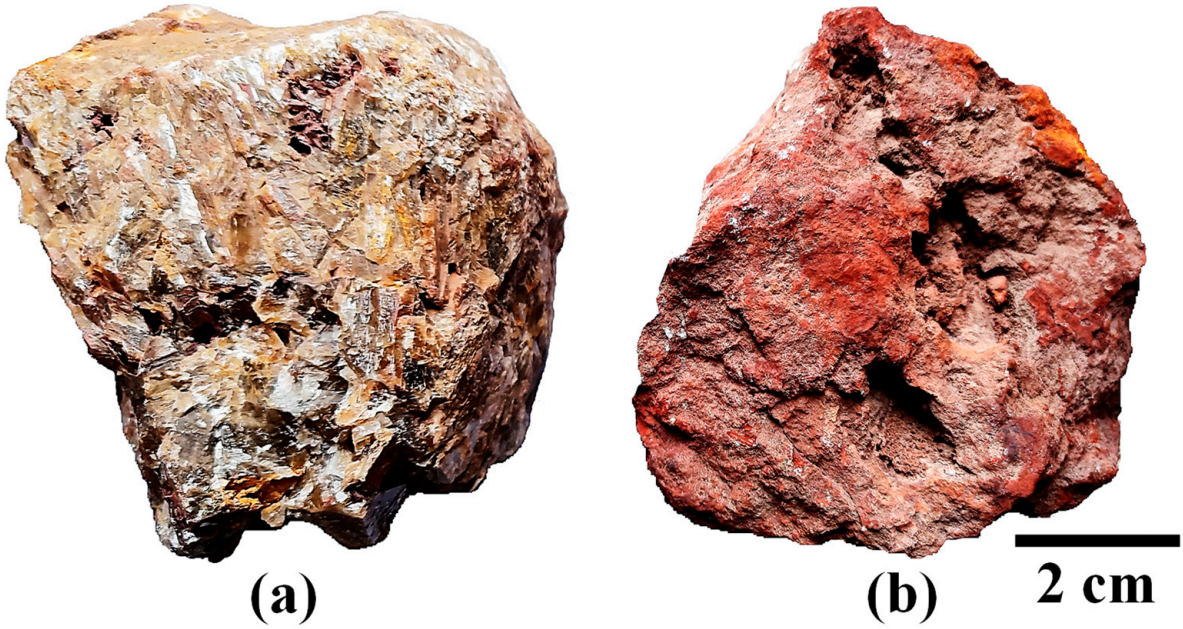

Figure 3. Hand specimens of the studied samples: (**a**) barite and (**b**) hematite.

3. Materials and Methods

3.1. Materials

As shown in Figure 1, the location map illustrates the Ghorabi and El Gedida mines in the Baharia Oases in the Western Desert, where the representative samples of barite and hematite were collected, respectively.

3.2. Material Preparation

The barite and hematite samples were washed, and then dried to dispose of the harmful materials. Then, each mineral was cut into six blocks with thicknesses of 2, 4, 6, 8, 10, and 12 cm using a chop saw. After cutting them, the blocks were smoothed and flattened to guarantee the cohesion of the blocks without any gaps when they were collected.

3.3. Material Characterization

3.3.1. Mineralogical Characterization

The mineralogical description is essential not only for petrographic classification but also to accentuate the features influencing the physical, chemical, and mechanical behavior of the natural samples [53]. X-ray diffraction (XRD), transmitted-light microscopy (TLM), and reflected-light microscopy (RLM) are the most common techniques used to describe the mineralogical composition of mineral samples. Unlike TLM, RLM is specified to characterize the non-transmitted minerals known as ores. The samples were pulverized and sieved using a 230 mesh (63 μm) sieve before being measured using a Philips X-ray diffractometer (XRD, Mod. PW 139) with Ni-filtered Cu-Kα radiation. The XRD patterns were obtained between 4 and 70° 2θ with a step size of 0.020° within a step time of 0.4 s. According to BS EN 12407:2007 [53], thin and polished sections of minerals were prepared to be examined by TLM and RLM using a digital camera, respectively.

3.3.2. Morphological Characterization

The powdered samples (<63 μm) were dried at 60 °C, and then, they were coated with platinum under vacuum for their examination by scanning electron microscopy (SEM, Beam energy: 20–30 kV, JSM-6700F, JEOL Ltd., Tokyo, Japan) with secondary electron (SE) imaging to identify the morphology and grain shape of the minerals visually.

3.3.3. Physical and Mechanical Characterization

In terms of the physical properties, the addressed minerals were considered to be dimension stones as they were fabricated in specific sizes or shapes [54]. Moreover, density and water absorption are the most significant physical properties, which characterize these types of samples as a measure of their specific gravity and porosity, respectively. Therefore, the density and water absorption were measured in compliance with ASTM C97 [55]. The Brunauer–Emmett–Teller (BET) method was applied to detect the surface area of the samples using the N2-adsorption–desorption isotherm (BET), which was determined using a BET Multi-point (St 2 on NOVA touch 4LX (s/n:17016062702), Quantachrome Instruments, Boynton Beach, FL, USA) [56]. Relating to the mechanical properties of the samples, they were evaluated by measuring both the crushing and impact values following BS 812-110 and BS 812-112 [57,58], respectively.

3.3.4. Geochemical Characterization

According to ASTM E1621 and D7348 [59,60], an Axios Sequential Wavelength Dispersive X-Ray Fluorescence (WDXRF) Spectrometer (Mod. Connolly, 2005/PANalytical, Almelo, The Netherlands) was employed to describe the geochemical features of the samples (<63 μm) as this is one of the essential parameters controlling radiation attenuation [61]. Additionally, XRF provides the elemental composition that is necessary as an input file in the theoretical calculations by the NXcom program.

3.4. Radiation Attenuation

3.4.1. Radiation Measurements

The radiation measurements were performed at the Nuclear Research Center (Egyptian Atomic Energy Authority). The mineral blocks were irradiated by a collimated beam emitted by PuBe (with activity of 185 GBq) based on a fine beam geometry setup, which was conducted to evaluate their shielding capacity against fast neutrons and γ-rays. A stilbene organic scintillator with the dimensions of 40 mm (diameter) × 40 mm (thick) with a 6 mm slit was used to detect the transmitted radiation beam behind the samples. As shown in Figure 4, the source was set at a distance of 400 mm from the detector. To protect the detector from the background radiation, the detector was enclosed by a lead shield, and the experiment set-up was positioned in the middle of the room. In all of the radiation measurements, the mineral blocks were positioned 50 mm away from the PuBe source (Figure 4). To obtain the needed thicknesses, some blocks were experimented on alone (e.g., 20, 40, and 60 mm) or together (e.g., 80 and 100 mm). The assembled blocks were flattened to avert cavities or gaps, which would worsen the shielding effectiveness.

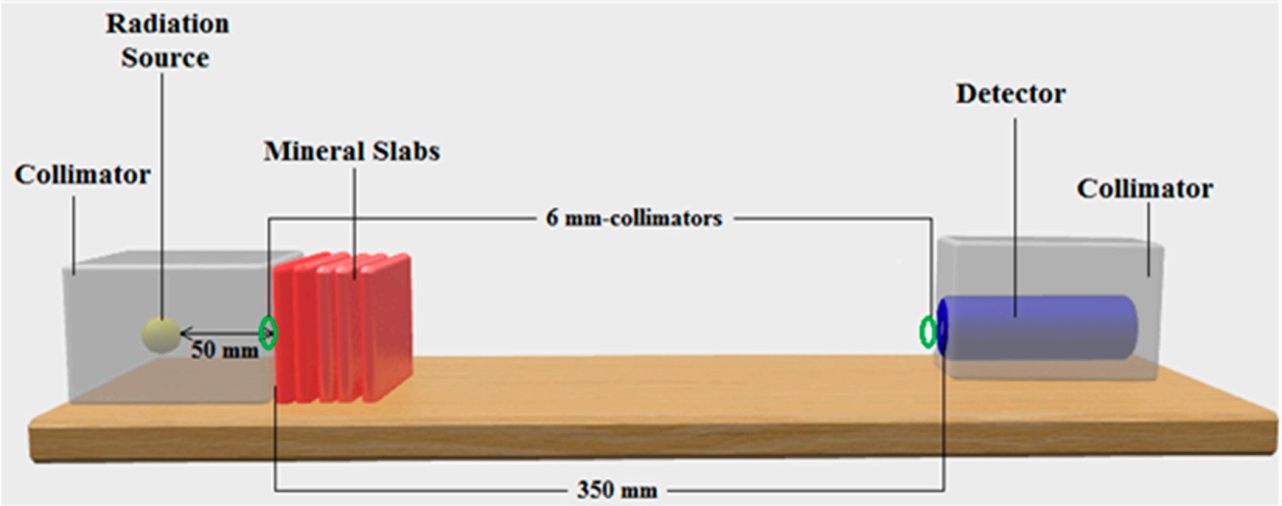

Figure 4. Experimental setup of the radiation measurements.

Through the anticoincidence mode with a zero cross-over method, a pulse shape discrimination (PSD) was conducted to process the recoil protons and electrons when the neutrons and γ-rays interacted with the scintillator, respectively [62]. So, neutrons and γ-rays can be differentiated [63]. The γ-ray spectra at 4.43 and 3.92 MeV produced from PuBe as well as those at 0.661 and 1.332 MeV from ^{137}Cs and ^{60}Co, respectively, were employed to calibrate the stilbene detector. The working energy ranges of the PuBe source for the fast neutrons and γ-rays were 0.8–11 and 0.4–8.3 MeV, respectively. The counting time was adjusted to maintain statistical uncertainty. A digital counter was accompanied by a high operating voltage of −1900 V to detect the energy instabilities of the radiation source. As shown in Figure 5, the planning arrangement of the experiment included the electronic devices of the neutron–gamma spectrometer with the dynode collections of the photomultiplier tube.

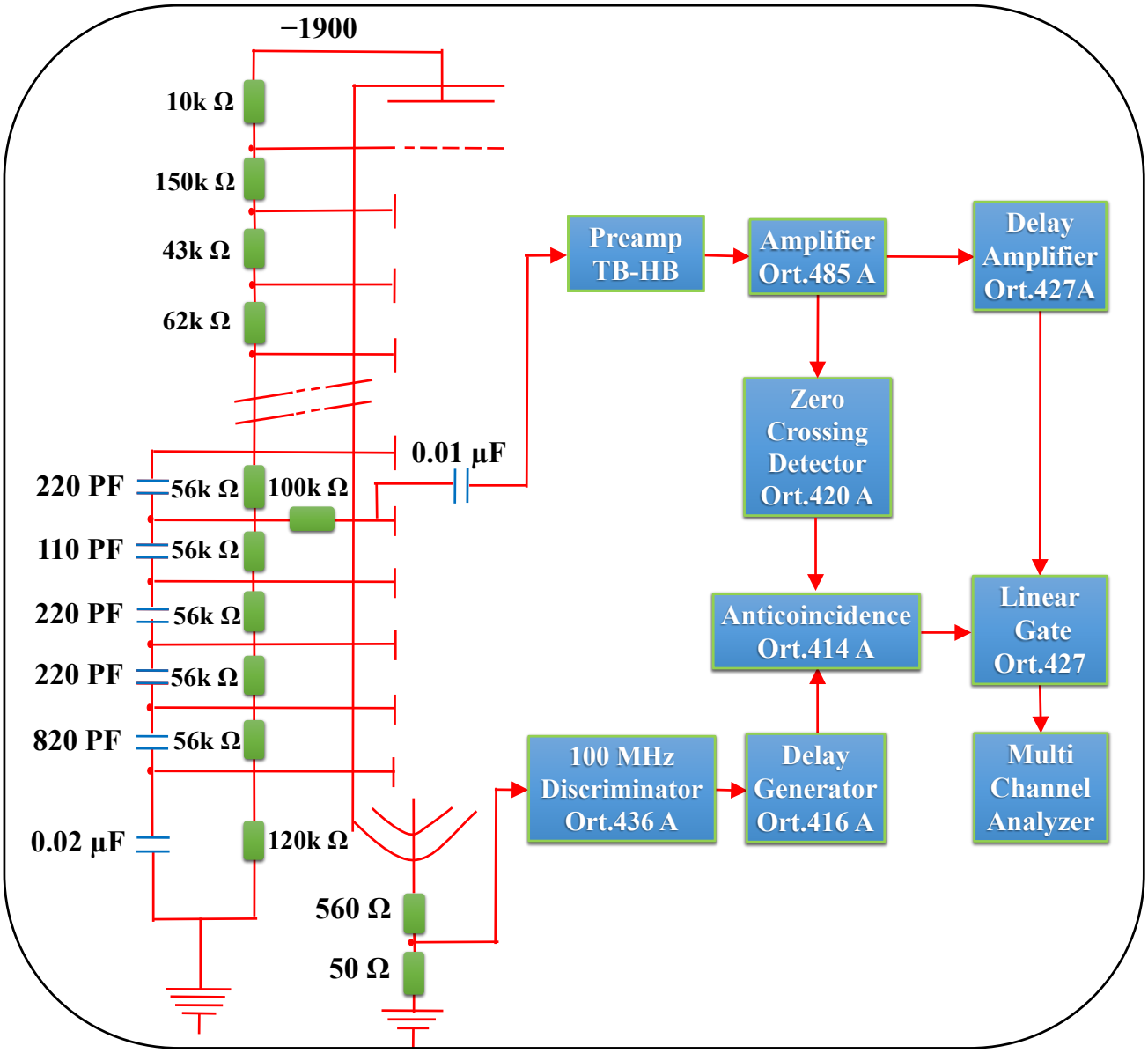

Figure 5. A block diagram of the experimental design showing the electronic device of a fast neutron–gamma spectrometer with dynode collections of the photomultiplier tube.

Table 1 lists Equations (1)–(4) which were applied to determine the necessary parameters for assessing the radiation attenuation efficiency against the fast neutrons and γ-rays. The propagated statistical uncertainties were evaluated to be under 10% using Equations (5) and (6).

Table 1. Equations employed to determine the different attenuation parameters of fast neutrons and γ-rays, as well as uncertainty propagation equations.

No.	Parameter	Symbol	Unit	Description	Equation		Abbreviations
1	Effective Macroscopic removal cross-section of fast neutrons	Σ_R	cm^{-1}	Probability of fast neutron to undergo a first collision removing it from the group of penetrating, uncollided neutrons	$N = N_o e^{-\Sigma_R x}$	(1)	N_0 and N are incident and transmitted intensities for fast neutrons, respectively, within the energy range of 0.8–11 MeV; *x*: sample thickness in cm.
2	Linear attenuation coefficient of γ-rays	μ	cm^{-1}	Fraction of attenuated incident photons per unit thickness of a material	$I = I_0 e^{-\mu x}$	(2)	I_0 and I are incident and transmitted intensities for total γ-rays, respectively, within the energy range of 0.4–8.3 MeV
3	Mean free path	MFP	cm	Average distance between the two successive interactions	$MFP = 1/\Sigma_R, 1/\mu$	(3)	
4	Half value layer	HVL	cm	Thickness reducing the radiation intensity to half	$HVL = \ln 2/\Sigma_R, \ln 2/\mu$	(4)	
5	Uncertainty propagation equations				$\Delta(\mu) = \frac{1}{x}\sqrt{\left(\frac{\Delta I_o}{I_o}\right)^2 + \left(\frac{\Delta I}{I}\right)^2 + \left(\ln\frac{I_o}{I}\right)^2\left[\left(\frac{\Delta\rho}{\rho}\right)^2 + \left(\frac{\Delta x}{x}\right)^2\right]}$	(5)	ρ: sample density
6					$\Delta(\Sigma_R) = \frac{1}{x}\sqrt{\left(\frac{\Delta N_o}{N_o}\right)^2 + \left(\frac{\Delta N}{N}\right)^2 + \left(\ln\frac{N_o}{N}\right)^2\left[\left(\frac{\Delta\rho}{\rho}\right)^2 + \left(\frac{\Delta x}{x}\right)^2\right]}$	(6)	

3.4.2. Theoretical Calculations (NXcom)

The NXcom program was applied in this study, using the elemental compositions and density values as an input file to calculate the fast removal cross-section (Σ_R) of the addressed shield material [64]. NXcom is a computational program developed by El-Khayatt to calculate Σ_R based on the "Mixture Rule" according to the following equation [65]:

$$\Sigma_R = \sum_i w_i (\Sigma_R)_i$$

where w_i and $(\Sigma_R)_i$ are related to the fractional weight and the fast neutron macroscopic removal cross-section of the *i*th element constituting the samples, respectively.

4. Results and Discussion

4.1. Mineralogical Characterization

The XRD analyses, supported by the 2θ values of each peak position, show that the barite and hematite minerals are the main constituents of the two samples (Figure 6). Insignificant appearances of calcite, hematite, and quartz minerals are present in the barite sample, while insignificant amounts of alunite, goethite, quartz, and barite are associated with hematite sample. Figure 7 illustrates the different photomicrographs taken when we conducted optical microscopy in two examination positions, plane-polarized light (PPL) and crossed-polarized light (CPL), confirming the mineral association of XRD. As for the microscopic examination of the barite sample, euhedral and clear crystals of barite are present with some fracture-filling Fe oxides (i.e., hematite), as illustrated in Figure 7a,b. Additionally, tiny grains of quartz are randomly present in the fractures between the barite crystals (Figure 7c). As for the hematite sample, Figure 7d illustrates white colloform bands of hematite, indicating the hydrothermal origin of this mineral, and this was also stated by Baioumy et al. [43]. These hematite bands are intersected by a grey veinlet of barite.

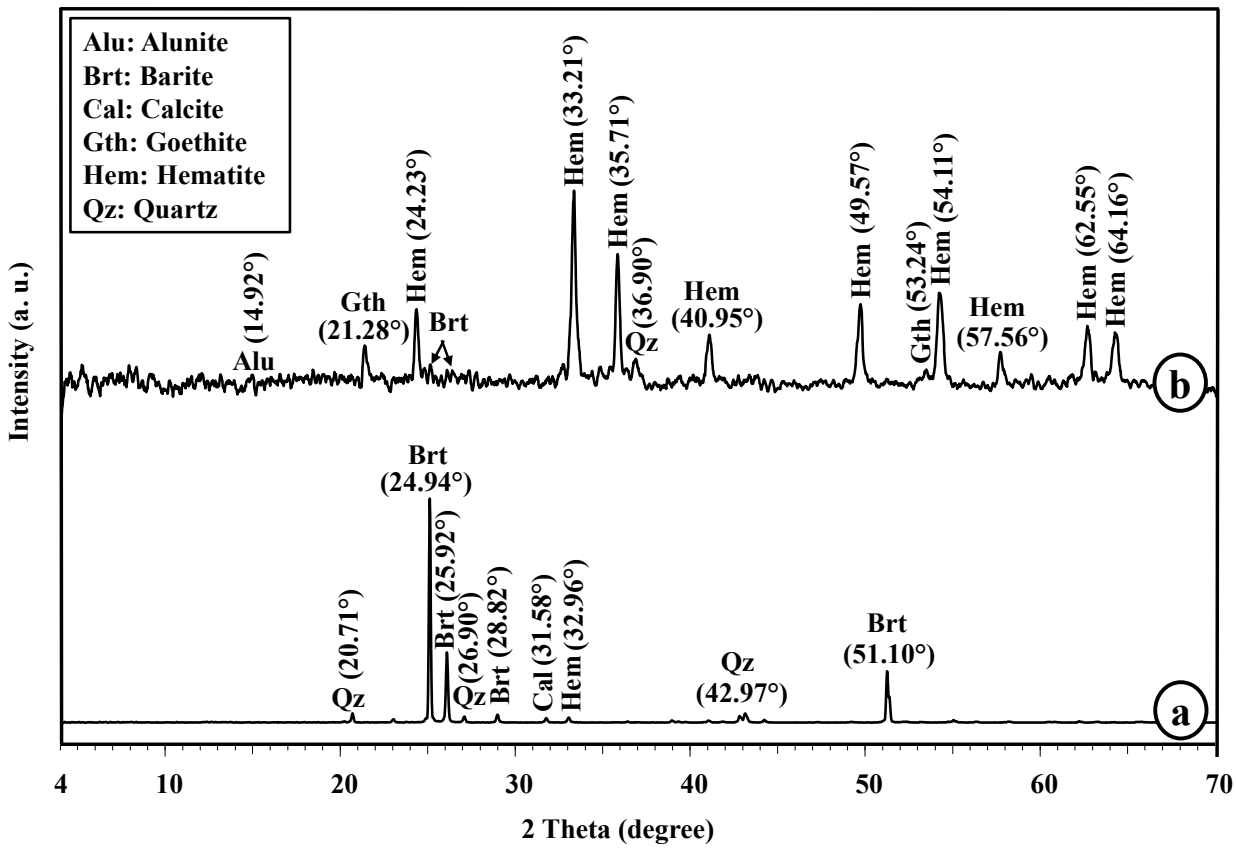

Figure 6. XRD charts of the studied samples showing the constituent mineral phases with their 2θ values of peak positions: (**a**) barite sample and (**b**) hematite sample.

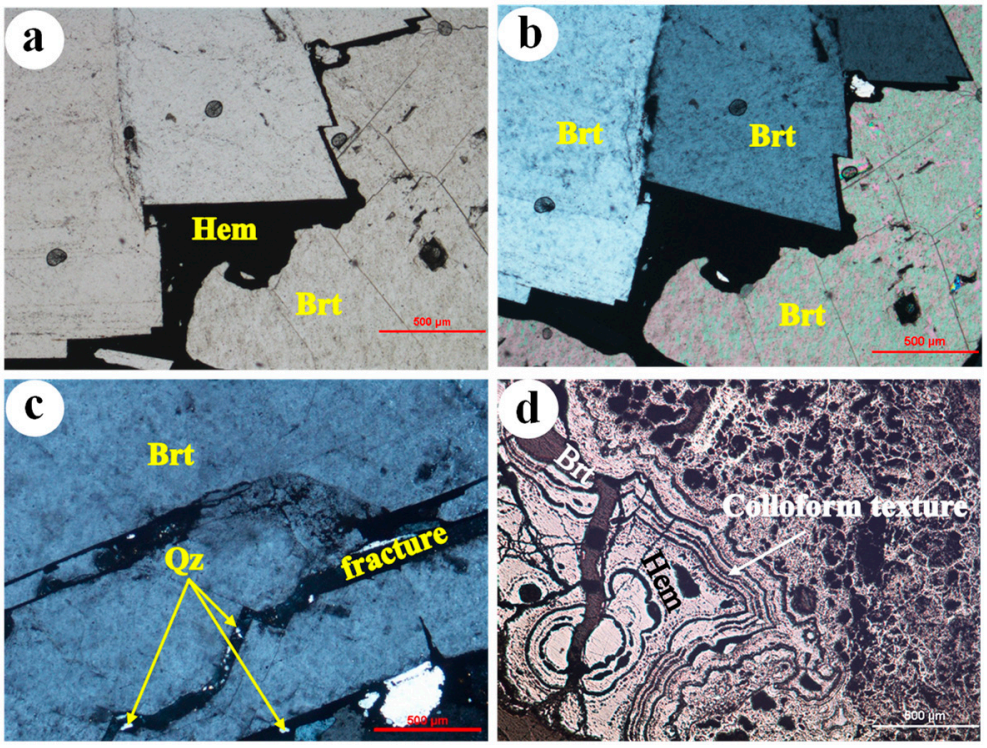

Figure 7. Photomicrographs taken by TLM (**a**–**c**) and RLM (**d**) in PPL (**a**) and CPL (**b**–**d**): (**a**–**c**) euhedral barite (Brt) grains with hematite (Hem) and quartz (Qz) minerals filling fractures, and (**d**) white colloform bands of Hem intersected by grey Brt veinlet.

4.2. Morphological Characterization

The SEM images confirm the findings of the TLM, including the euhedral forms of orthorhombic-shaped barite particles. These euhedral orthorhombic particles allow for more compacting and fewer intra-particle pores in the mineral structure (Figure 8a). Additionally, the magnified image shows very fine sub-spherical or botryoidal particles of hematite on the barite surface (Figure 8b). These findings are corroborated by those of previous studies [66]. On the other hand, Figure 8c,d shows the hematite particles with a botryoidal shape, which permits there to be more pores between the particles, producing a less compacted structure in the hematite sample compared to that in the barite one. This shape could have a detrimental effect on the radiation shielding properties of these minerals.

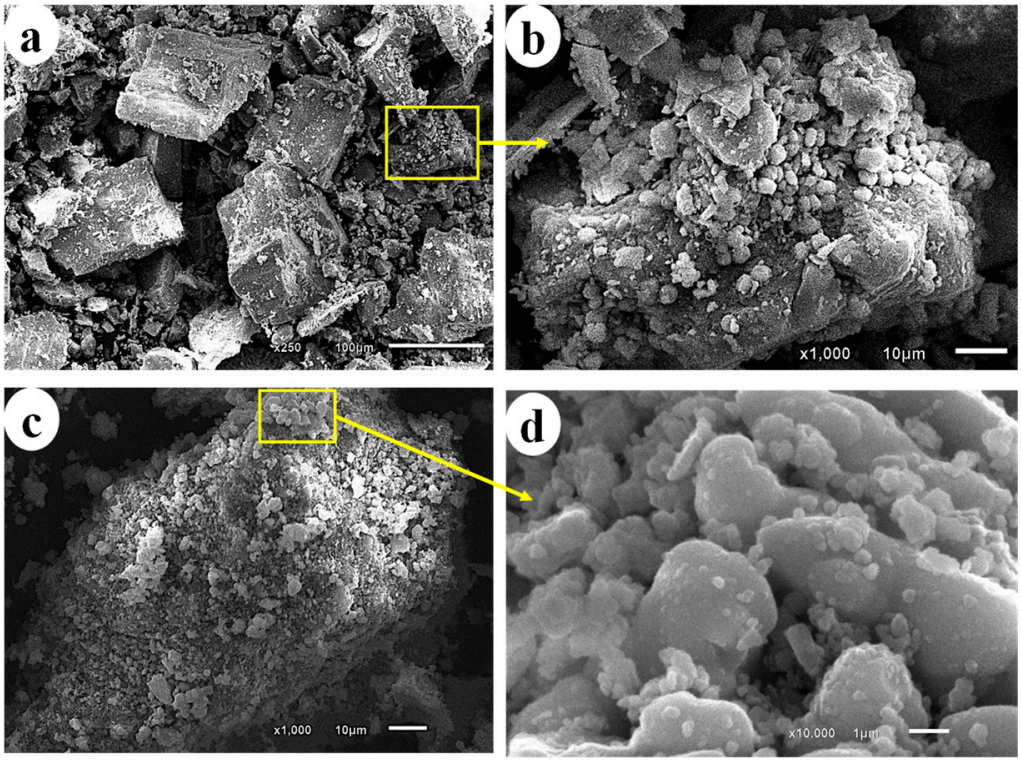

Figure 8. SEM images showing the surface morphology of the studied samples: (**a**,**b**) euhedral orthorhombic crystals of barite minerals associated with sub-spherical hematite were found in the barite sample, and (**c**,**d**) botryoidal-shaped particles of hematite.

4.3. Physical and Mechanical Characterization

The physical tests of the studied samples (Table 2) demonstrate that the barite sample has a higher density (4.2 g/cm^3) than the hematite one has (2.9 g/cm^3). This can be assigned to the higher compactness of the particles in the barite structure than those in the hematite one, as was mentioned before and is illustrated by the SEM images (Figure 8). Otherwise, the water absorption capacity of the barite sample (1.07%) is less than that of hematite (12.31%). This is also ascribed to the higher density and lower porosity of barite compared to hematite. Additionally, the surface area analysis reveals that the hematite has a larger surface area (3.50 m^2/g) than the barite sample does (2.12 m^2/g). This can be attributed to the botryoidal habit of the hematite particles compared to the orthorhombic habit of the barite ones (Figure 8). This larger surface area accounts for the higher water absorption capacity of hematite (12.31%) compared to that of barite (1.07%). Based on the results of the mechanical properties, the barite sample exhibits higher crushing and impact values (42.5 and 41%) than the hematite sample does (7.70 and 6.80%). This indicates the lower strength of barite compared to the hematite sample. This difference in the sample strength can be

attributed to the stronger Fe–O bond in the hematite compared to the S–O bond in the sulfate group of the barite. Therefore, barite is not recommended as a principal aggregate in concrete.

Table 2. Physical and mechanical properties of the studied samples.

Property	Barite	Hematite	International Standard
Density (g/cm^3)	4.20	2.90	ASTM C97 [55]
Water absorption (%)	1.07	12.31	ASTM C97 [55]
Surface area (m^2/g)	2.12	3.50	BET method [56]
Crushing value (%)	42.50	7.70	BS 812-110 [57]
Impact value (%)	41.00	6.80	BS 812-112 [58]

4.4. Geochemical Characterization

Table 3 summarizes the chemical compositions of the two addressed mineral samples. The main composition of the barite sample comprised four principal oxides, including BaO, SO_3, Fe_2O_3, and SiO_2, with quantities of 57.89, 29.55, 6.79, and 2.03%, respectively. The high proportions of BaO and SO_3 are due to the presence of barite minerals, which consist of $BaSO_4$. As for the ratio of Fe_2O_3, the reason for it is due to the association of some iron oxyhydroxides, such as hematite or goethite, as illustrated in the TLM images (Figure 7). On the other hand, the minor oxides of SiO_2, CaO, Al_2O_3, and MgO with quantities of 2.03, 0.66, 0.64, and 0.38%, could be ascribed to the presence of clay deposits, which are associated with barite [45]. Otherwise, the presence of SiO_2, Al_2O_3, and CaO may also be credited to the presence of the gangue minerals of quartz (SiO_2), alunite [$KAl_3(SO_4)_2(OH)_6$], and calcite ($CaCO_3$), respectively. These findings are in agreement with those of previous studies [45]. The lower LOI% (1.16%) may be attributed to the minor presence of goethite and alunite minerals. This low LOI% can also be attributed to the presence of the calcite mineral. Concerning the hematite sample, the high amount of Fe_2O_3 (87.32%) is assigned to the high presence of the hematite mineral, and to a lesser extent, goethite and iron oxyhydroxide FeO(OH), as was assured by XRD data (Figure 6). The minor quantities of SiO_2 and SO_3 in the hematite sample can be ascribed to the low occurrences of quartz and barite minerals, respectively. As reported previously by Baioumy et al. [43], the lower quantity of MnO_2 (0.79%) in the hematite ore is attributed to the associated hydrothermal solutions. The presence of the major minerals (i.e., barite and hematite) and some minor minerals (i.e., calcite, quartz, and hematite) was confirmed by the XRD (Figure 6) and TLM (Figure 7).

Table 3. XRF analysis of the studied samples.

Oxide (%)	Barite	Hematite
MgO	0.38	0.18
SiO_2	2.03	2.05
Fe_2O_3	6.79	87.32
CaO	0.66	0.12
Al_2O_3	0.64	1.11
BaO	57.89	0.98
SO_3	29.55	1.22
K_2O	0.02	0.02
Na_2O	0.42	0.42
TiO_2	0.01	0.02
MnO_2	0.20	0.79
P_2O_5	0.03	0.30
SrO	0.01	0.01
NiO	0.01	0.00
ZnO	0.00	0.10
LOI	1.16	5.34

4.5. Radiation Attenuation

4.5.1. Fast Neutron Attenuation

Figure 9 demonstrates a linear relationship between ln (N_0/N) and the sample thickness which is consistent with the Beer–Lambert law. From these relationships, the experimental macroscopic removal cross-section of the fast neutrons ($\Sigma_{R,ex.}$, cm^{-1}) for each sample was attained. As shown in Table 4, the measured fast neutron attenuation parameters, including the $\Sigma_{R,ex.}$ (cm^{-1}), MFP (cm), and HVL (cm) of the barite sample are better than those of the hematite sample by about 9.17%. The higher density (4.20 g/cm^3) and compacted morphology of it (Figure 8a) compared to those of the hematite sample (i.e., lower density, 2.90 g/cm^3 and less compacted morphology) account for the superiority of the barite sample in neutron attenuation. This can be attributed to the fact that the higher density and lower porosity of material allow for more potency in the inelastic and elastic collisions to slow down the fast neutrons [25]. As shown in Table 4, the NXcom calculation illustrates that the fast neutron attenuation of the barite sample is higher than that of the hematite sample by 12.25%. Moreover, there is a satisfactory agreement between the NXcom results and the measurements of the fast neutron attenuation, as shown in Table 4. More specifically, the measured results are lower than the NXcom findings by about 16 and 19.25% for barite and hematite, respectively. This difference can be credited to the irregularities in the sample thicknesses, the source power, the radiation background, or the inaccuracy in the elemental composition.

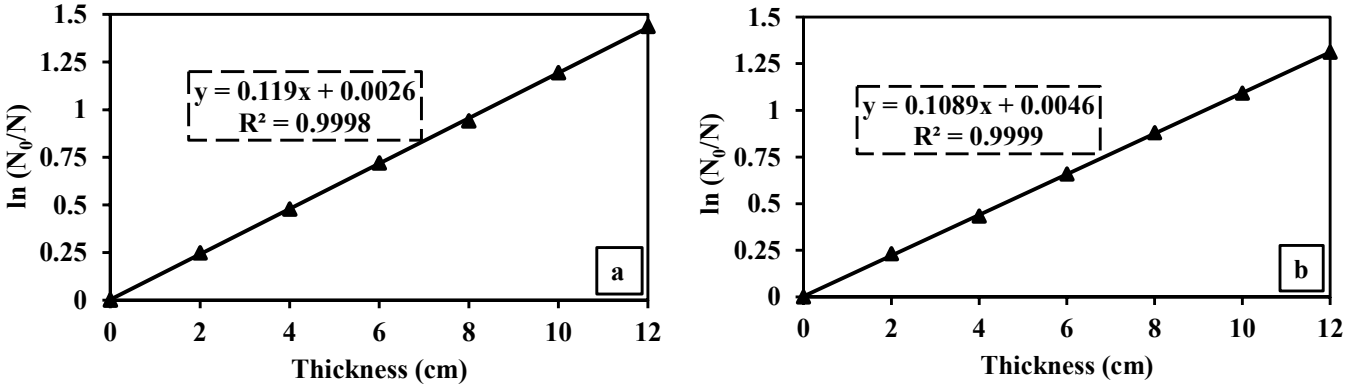

Figure 9. Variation of ln (N_0/N) with different thicknesses (0, 2, 4, 6, 8, 10, and 12 cm) of samples of (**a**) barite and (**b**) hematite at neutron energy value of 0.8–11 MeV.

Table 4. Experimental fast neutron attenuation parameters measured behind PuBe with statistical uncertainty correlated with their corresponding theoretical (NXcom) values.

Sample Type	Experimental			Theoretical (NXcom)			Dev. (%) *
	Σ_R (cm^{-1})	MFP (cm)	HVL (cm)	Σ_R (cm^{-1})	MFP (cm)	HVL (cm)	
Barite	0.119 ± 0.010	8.330 ± 0.580	5.780 ± 0.400	0.1026	9.750	6.760	16.00
Hematite	0.109 ± 0.009	9.170 ± 0.640	6.360 ± 0.450	0.0914	10.940	7.580	19.25

* Dev. (%) = [Σ_R (experimental) − Σ_R (theoretical)] × 100/Σ_R (experimental).

4.5.2. γ-Rays

As in the fast neutrons (Figure 9), Figure 10 reveals a linear relationship between ln (I_0/I) and the sample thicknesses, which follows the Beer–Lambert law. From these relationships, the linear attenuation coefficient of the γ-rays (μ, cm^{-1}) for each sample has been attained. As shown in Table 5, the values of μ, cm^{-1}, and the other γ-ray attenuation parameters (i.e., MFP and HVL) are listed. Similar to the fast neutron attenuation, these attenuation parameters demonstrate that the efficiency of the γ-ray attenuation of the barite sample shows superiority over its corresponding hematite one. Moreover, the γ-ray

attenuation efficiency of the barite sample is higher than that of the hematite sample by about 51%. This can be attributed to the following: (1) the barite sample has a higher density and compactness than the hematite sample does (Table 2 and Figure 8), which is in agreement with [67], (2) the barite sample is mainly composed of barium (Ba), which has a higher atomic number (Z = 56) than iron (Z = 26), which is the main component of the hematite sample (Table 3), and (3) in the hematite sample, the high secondary γ-ray emissions from PuBe contributed to the deterioration of the attenuation capacity as a result of (a) the inelastic scattering of the fast neutrons with different energies inside the sample [68], (b) the neutron interactions especially of energies >0.5 MeV with Fe nuclei, and (c) the radiative capture of the slow neutrons [69].

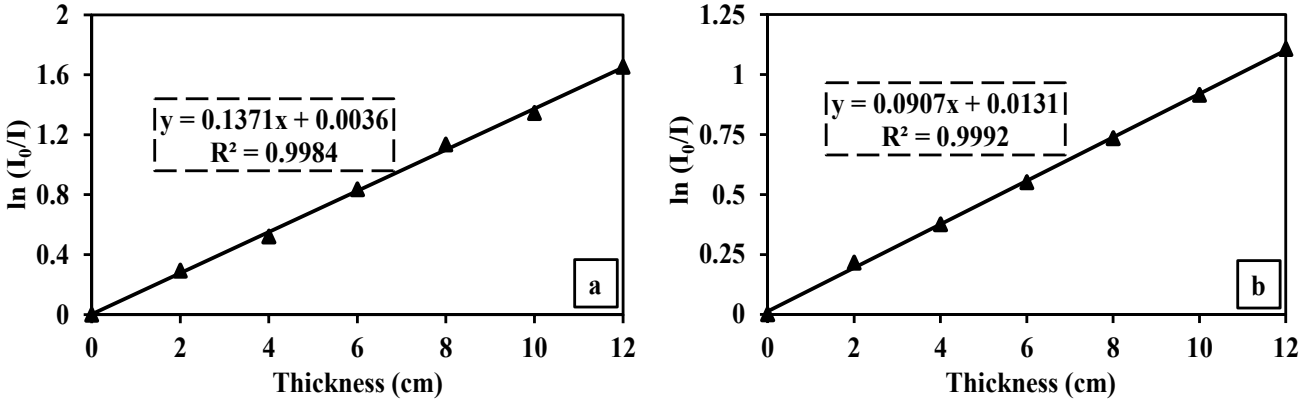

Figure 10. Variation of ln (I_0/I) with different thicknesses (0, 2, 4, 6, 8, 10, and 12 cm) of samples of (**a**) barite and (**b**) hematite at a photon energy value of 0.4–8.3 MeV.

Table 5. Experimental γ-ray attenuation parameters measured behind PuBe with statistical uncertainty.

Sample Type	μ (cm^{-1})	MFP (cm)	HVL (cm)
Barite	0.1370 ± 0.0140	7.300 ± 0.510	5.060 ± 0.150
Hematite	0.0907 ± 0.0090	10.990 ± 0.660	7.620 ± 0.380

4.5.3. Radiation Attenuation Comparison

The radiation attenuation efficiencies of the current investigated samples were compared to that of other previously studied samples, which were investigated under similar experimental conditions. The description of the compared samples from the previous studies is exhibited in Table 6, while the comparison of their attenuation efficiency is illustrated in Figure 11. It was found that the barite sample shows a higher fast neutron attenuation rate than the concrete mixes of A, AB1, AB2, AH25, LBC, and CBC did, while the hematite sample has a higher fast neutron attenuation rate than the same previous concrete mixes did, except for AH25. Moreover, the γ-attenuation of the barite sample exhibits superiority over all of the compared concrete mixes, while the hematite sample has a higher capability than the concrete mixes of A, AB1, AB2, AH25, LBC, and CBC do. This comparison confirms that barite and hematite can be eco-friendly and sustainable alternatives to some RSCs which require high cement production. This can be a significant means to reduce the production cost and significant emissions of greenhouse gases.

Table 6. Description of the compared samples of previous studies including different concrete mixes with the same conditions of radiation attenuation measurement.

Sample Code	Description	Ref.
A	Concrete totally composed of antigorite serpentine aggregate	[70]
AB1	Concrete composed of antigorite serpentine aggregate incorporated with 1% of boric acid by cement weight	
AB2	Concrete composed of antigorite serpentine aggregate incorporated with 3% of boric acid by cement weight	
AH25	Concrete composed of 75% antigorite serpentine aggregate + 25% hematite aggregate	[68]
AH50	Concrete composed of 50% antigorite serpentine aggregate + 50% hematite aggregate	
AB25	Concrete composed of 75% antigorite serpentine aggregate + 25% barite aggregate	
AB50	Concrete composed of 50% antigorite serpentine aggregate + 50% barite aggregate	
LBC	Concrete totally composed of lizardite serpentine aggregate	[71]
CBC	Concrete totally composed of chrysotile serpentine aggregate	

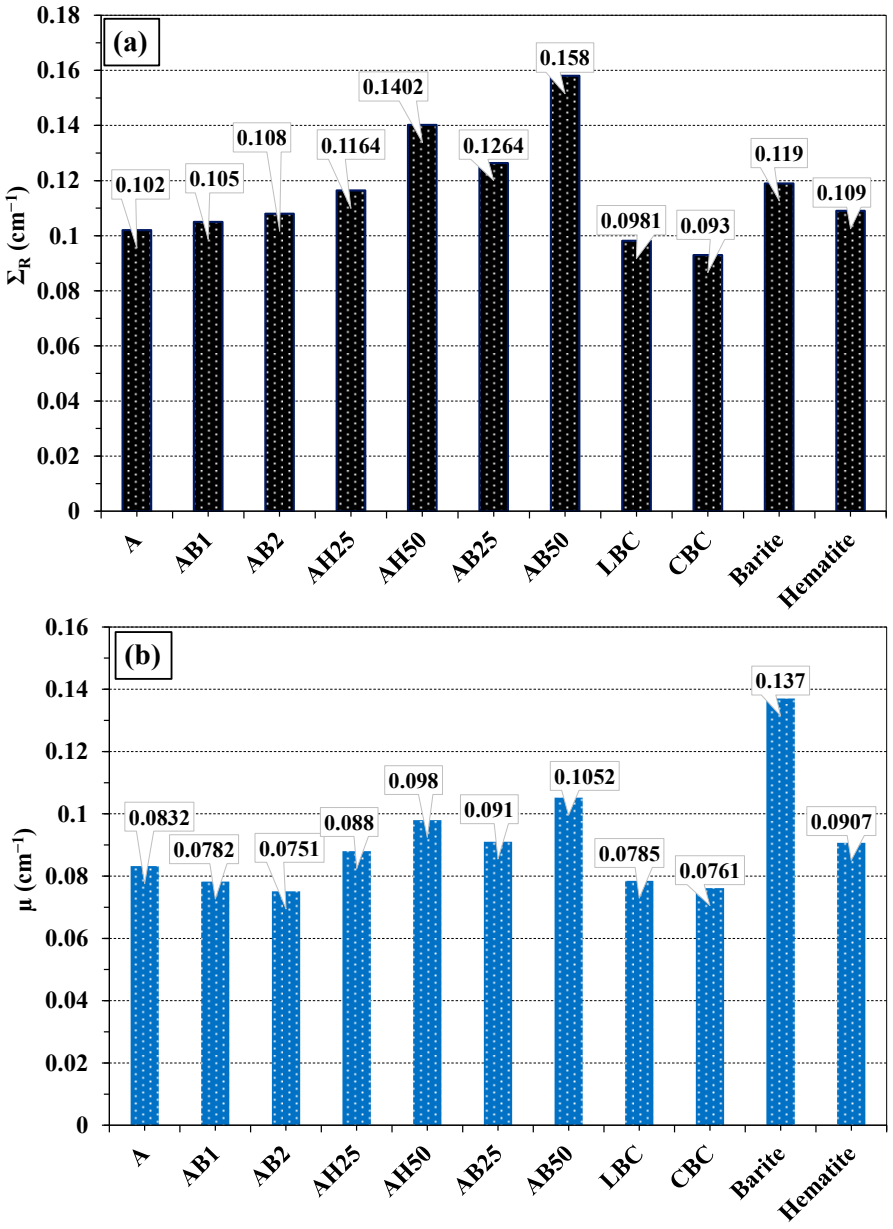

Figure 11. Comparison between the radiation attenuation of previously and currently studied samples against: (**a**) fast neutrons at the energy range of 0.8–11 MeV and (**b**) γ-rays at the energy range of 0.4–8.3 MeV.

5. Conclusions

Based on the outcomes of the recent study, the following conclusions can be drawn:

- Unlike the mechanical properties (i.e., crushing and impact values), the physical properties (i.e., density and water absorption) of barite are more enhanced than those of hematite.
- The dense structure of barite can be correlated to its orthorhombic-shaped grains, whereas the sub-spherical and botryoidal-shaped grains of hematite result in a decompressed structure.
- The radiation attenuation of barite against fast neutrons and γ-rays surpassed that of hematite by 12.25 and 51%, respectively.
- The high ratio of BaO (57.89%) and the densified structure of barite justify its higher radiation attenuation compared to that of hematite, which has a higher Fe_2O_3 % and a less compact structure.
- A considerable agreement was obtained between the experimental and theoretical calculations (NXcom) of the fast neutron attenuation for both the barite and hematite samples, with reasonable deviations of 16 and 19.25%, respectively.
- Compared to different concrete mixes, barite and hematite can be employed as natural, sustainable, and cost-effective alternatives to cement-consuming RSC.

Author Contributions: Conceptualization, M.A.M. and A.M.Z.; methodology, M.A.M.; software, A.M.E.-K.; validation, M.A.M., A.M.Z., M.W.M., M.A.R. and A.M.E.-K.; formal analysis, A.M.E.-K., M.W.M. and M.A.R.; investigation, M.A.M., A.M.Z., W.A. and A.M.E.-K.; resources, A.M.Z. and M.A.M. and W.A.; data curation, M.A.M., A.M.Z., W.A. and A.M.E.-K.; writing—original draft preparation, M.A.M., A.M.Z., A.M.E.-K., B.R.B. and M.G.S.; writing—review and editing, A.M.Z., A.M.E.-K., M.W.M. and M.A.R.; visualization, M.A.M., A.M.Z. and A.M.E.-K.; supervision, M.G.S., B.R.B., A.M.Z. and A.M.E.-K.; project administration A.M.E.-K.; funding acquisition, A.M.E.-K. All authors have read and agreed to the published version of the manuscript.

Funding: The authors extend their appreciation to the Deanship of Scientific Research at Imam Mohammad Ibn Saud Islamic University for funding this work through Research Group no. RG-21-09-43.

Institutional Review Board Statement: Not applicable.

Informed Consent Statement: Not applicable.

Data Availability Statement: The authors confirm that the data used to support the findings of this study are available within the article.

Conflicts of Interest: The authors declare no conflict of interest.

References

1. Lee, S.; Kim, M.; Lee, J. Analyzing the Impact of Nuclear Power on CO_2 Emissions. *Sustainability* **2017**, *9*, 1428. [CrossRef]
2. Mukherjee, S. *Applied Mineralogy: Applications in Industry and Environment*; Springer Science & Business Media: Berlin/Heidelberg, Germany, 2012. [CrossRef]
3. Salati, A.; Share Isfahani, H.; Roshanzamir, M.A.; Azhari, A. Investigating the effect of hematite additive on the performance of clay barriers for radioactive waste disposals. *Bull. Eng. Geol. Environ.* **2022**, *81*, 415. [CrossRef]
4. El-Samrah, M.G.; Tawfic, A.F.; Chidiac, S.E. Spent nuclear fuel interim dry storage; Design requirements, most common methods, and evolution: A review. *Ann. Nucl. Energy* **2021**, *160*, 108408. [CrossRef]
5. Ryan, J.L. Ionizing Radiation: The Good, the Bad, and the Ugly. *J. Investig. Dermatol.* **2012**, *132*, 985–993. [CrossRef] [PubMed]
6. El-Samrah, M.G.; Abdel-Rahman, M.A.E.; El Shazly, R.M. Effect of heating on physical, mechanical, and nuclear radiation shielding properties of modified concrete mixes. *Radiat. Phys. Chem.* **2018**, *153*, 104–110. [CrossRef]
7. Tekin, H.O.; Sayyed, M.I.; Issa, S.A.M. Gamma radiation shielding properties of the hematite-serpentine concrete blended with WO3 and Bi2O3 micro and nano particles using MCNPX code. *Radiat. Phys. Chem.* **2018**, *150*, 95–100. [CrossRef]
8. Sakr, K.; Ramadan, W.; Sayed, M.; El-Zakla, T.; El-Desouqy, M.; El-Faramawy, N. Utilization of barite/cement composites for gamma rays attenuation. *Radiat. Eff. Defects Solids* **2018**, *173*, 269–282. [CrossRef]
9. Azreen, N.M.; Rashid, R.S.M.; Mugahed Amran, Y.H.; Voo, Y.L.; Haniza, M.; Hairie, M.; Alyousef, R.; Alabduljabbar, H. Simulation of ultra-high-performance concrete mixed with hematite and barite aggregates using Monte Carlo for dry cask storage. *Constr. Build. Mater.* **2020**, *263*, 120161. [CrossRef]

10. Zeyad, A.M.; Hakeem, I.Y.; Amin, M.; Tayeh, B.A.; Agwa, I.S. Effect of aggregate and fibre types on ultra-high-performance concrete designed for radiation shielding. *J. Build. Eng.* **2022**, *58*, 104960. [CrossRef]
11. Sayyed, M.I.; Almousa, N.; Elsafi, M. Preparation of Mortar with Fe_2O_3 Nanoparticles for Radiation Shielding Application. *Coatings* **2022**, *12*, 1329. [CrossRef]
12. Öz, A.; Bayrak, B.; Kavaz, E.; Kaplan, G.; Çelebi, O.; Alcan, H.G.; Aydın, A.C. The radiation shielding and microstructure properties of quartzic and metakaolin based geopolymer concrete. *Constr. Build. Mater.* **2022**, *342*, 127923. [CrossRef]
13. Abdullah, M.A.H.; Rashid, R.S.M.; Amran, M.; Hejazii, F.; Masenwat, N.A.B.; Fediuk, R.; Voo, Y.L.; Vatin, N.I.; Idris, M.I. Recent Trends in Advanced Radiation Shielding Concrete for Construction of Facilities: Materials and Properties. *Polymers* **2022**, *14*, 2830. [CrossRef] [PubMed]
14. Dąbrowski, M.; Jóźwiak-Niedźwiedzka, D.; Bogusz, K.; Glinicki, M.A. Influence of serpentinite aggregate on the microstructure and durability of radiation shielding concrete. *Constr. Build. Mater.* **2022**, *337*, 127536. [CrossRef]
15. Daungwilailuk, T.; Yenchai, C.; Rungjaroenkiti, W.; Pheinsusom, P.; Panwisawas, C.; Pansuk, W. Use of barite concrete for radiation shielding against gamma-rays and neutrons. *Constr. Build. Mater.* **2022**, *326*, 126838. [CrossRef]
16. Jaha, N.; Islam, G.M.S.; Kabir, M.F.; Khandaker, M.U.; Chowdhury, F.-U.-Z.; Bhuian, A.K.M.S.I. Ionizing radiation shielding efficacy of common mortar and concrete used in Bangladeshi dwellings. *Case Stud. Constr. Mater.* **2022**, *17*, e01547. [CrossRef]
17. Lv, Y.; Qin, Y.; Wang, J.; Li, G.; Zhang, P.; Liao, D.; Xi, Z.; Yang, L. Effect of incorporating hematite on the properties of ultra-high performance concrete including nuclear radiation resistance. *Constr. Build. Mater.* **2022**, *327*, 126950. [CrossRef]
18. Luo, L.; Chen, Z.; Tao, Q.; Xie, L.; Jin, D.; Li, Z.; Deng, D. Effects of high temperatures on the splitting tensile strength and gamma ray shielding performance of radiation shielding concrete. *Constr. Build. Mater.* **2022**, *343*, 127953. [CrossRef]
19. Amin, M.N.; Ahmad, I.; Iqbal, M.; Abbas, A.; Khan, K.; Faraz, M.I.; Alabdullah, A.A.; Ullah, S. Computational AI Models for Investigating the Radiation Shielding Potential of High-Density Concrete. *Materials* **2022**, *15*, 4573. [CrossRef]
20. Al-Buriahi, M.S.; Sayyed, M.; Bantan, R.A.; Al-Hadeethi, Y. Nuclear Radiation Shielding Characteristics of Some Natural Rocks by Using EPICS2017 Library. *Materials* **2021**, *14*, 4669. [CrossRef]
21. Khater, G.A.; Saudi, H.A.; Abd-Allah, W.M. Glass and Glass-Ceramics Based on Weathered Basaltic Rock for Radiation Shielding Applications. *Silicon* **2022**, *14*, 7449–7459. [CrossRef]
22. Aita, R.S.; Abdel Ghany, H.A.; Ibrahim, E.M.; El-Feky, M.G.; El Aassy, I.E.; Mahmoud, K.A. Gamma-rays attenuation by mineralized siltstone and dolostone rocks: Monte Carlo simulation, theoretical and experimental evaluations. *Radiat. Phys. Chem.* **2022**, *198*, 110281. [CrossRef]
23. Yılmaz, D.; Kılıc, A.D.; Kalecik, S. Radiation shielding parameters and Micro-Raman spectral analysis of some pyroclastic rocks. *Radiat. Phys. Chem.* **2023**, *203*, 110596. [CrossRef]
24. Hemid, E.M.; Kántor, T.; Tamma, A.A.; Masoud, M.A. Effect of groundwater fluctuation, construction, and retaining system on slope stability of Avas Hill in Hungary. *Open Geosci.* **2021**, *13*, 1139–1157. [CrossRef]
25. Çelen, Y.Y.; Akkurt, I.; Ceylan, Y.; Atçeken, H. Application of experiment and simulation to estimate radiation shielding capacity of various rocks. *Arab. J. Geosci.* **2021**, *14*, 1471. [CrossRef]
26. Masoud, M.A.; Rashad, A.M.; Sakr, K.; Shahien, M.G.; Zayed, A.M. Possibility of using different types of Egyptian serpentine as fine and coarse aggregates for concrete production. *Mater. Struct.* **2020**, *53*, 87. [CrossRef]
27. Mansour, A.; Sayyed, M.I.; Mahmoud, K.A.; Şakar, E.; Kovaleva, E.G. Modified halloysite minerals for radiation shielding purposes. *J. Radiat. Res. Appl. Sc.* **2020**, *13*, 94–101. [CrossRef]
28. Abu El-Soad, A.M.; Sayyed, M.I.; Mahmoud, K.A.; Şakar, E.; Kovaleva, E.G. Simulation studies for gamma ray shielding properties of Halloysite nanotubes using MCNP-5 code. *Appl. Radiat. Isot.* **2019**, *154*, 108882. [CrossRef]
29. Akkurt, I.; Kilincarslan, S.; Basyigit, C. The photon attenuation coefficients of barite, marble and limra. *Ann. Nucl. Energy* **2004**, *31*, 577–582. [CrossRef]
30. Oto, B.; Yıldız, N.; Akdemir, F.; Kavaz, E. Investigation of gamma radiation shielding properties of various ores. *Prog. Nucl. Energy* **2015**, *85*, 391–403. [CrossRef]
31. Dong, M.; Zhou, S.; Xue, X.; Sayyed, M.I.; Tishkevich, D.; Trukhanov, A.; Wang, C. Study of comprehensive shielding behaviors of chambersite deposit for neutron and gamma ray. *Prog. Nucl. Energy* **2022**, *146*, 104155. [CrossRef]
32. Eke, C.; Agar, O.; Segebade, C.; Boztosun, I. Attenuation properties of radiation shielding materials such as granite and marble against γ-ray energies between 80 and 1350 keV. *Radiochim. Acta* **2017**, *105*, 851–863. [CrossRef]
33. Mavi, B. Experimental investigation of γ-ray attenuation coefficients for granites. *Ann. Nucl. Energy* **2012**, *44*, 22–25. [CrossRef]
34. Masoud, M.A.; El-Khayatt, A.M.; Shahien, M.G.; Bakhit, B.R.; Suliman, I.I.; Zayed, A.M. Radiation Attenuation Assessment of Serpentinite Rocks from a Geological Perspective. *Toxics* **2022**, *10*, 697. [CrossRef]
35. Kunchariyakun, K.; Sukmak, P. Utilization of garnet residue in radiation shielding cement mortar. *Constr. Build. Mater.* **2020**, *262*, 120122. [CrossRef]
36. Marquez-Mata, C.A.; Mata Chavez, M.J.; Campillo-Rivera, G.E.; Vazquez-Bañuelos, J.; Garcia-Duran, A.; Vega-Carrillo, H.R. Shielding features of seven types on natural quartz. *Appl. Radiat. Isot.* **2021**, *167*, 109450. [CrossRef] [PubMed]
37. Singh, S.; Singh, K. On the use of green concrete composite as a nuclear radiation shielding material. *Prog. Nucl. Energy* **2021**, *136*, 103730. [CrossRef]

38. Zayed, A.M.; Masoud, M.A.; Rashad, A.M.; El-Khayatt, A.M.; Sakr, K.; Kansouh, W.A.; Shahien, M.G. Influence of heavyweight aggregates on the physico-mechanical and radiation attenuation properties of serpentine-based concrete. *Constr. Build. Mater.* **2020**, *260*, 120473. [CrossRef]
39. Akkurt, I.; El-Khayatt, A.M. The effect of barite proportion on neutron and gamma-ray shielding. *Ann. Nucl. Energy* **2013**, *51*, 5–9. [CrossRef]
40. Baioumy, H.M. Rare earth elements, S and Sr isotopes and origin of barite from Bahariya Oasis, Egypt: Implication for the origin of host iron ores. *J. Afr. Earth Sci.* **2015**, *106*, 99–107. [CrossRef]
41. Said, R. *The Geology of Egypt*, 1st ed.; Routledge: London, UK, 1990; p. 734. [CrossRef]
42. Salama, W.; El Aref, M.; Gaupp, R. Mineralogical and geochemical investigations of the Middle Eocene ironstones, El Bahariya Depression, Western Desert, Egypt. *Gondwana Res.* **2012**, *22*, 717–736. [CrossRef]
43. Baioumy, H.M.; Ahmed, A.H.; Khedr, M.Z. A mixed hydrogenous and hydrothermal origin of the Bahariya iron ores, Egypt: Evidences from the trace and rare earth element geochemistry. *J. Geochem. Explor.* **2014**, *146*, 149–162. [CrossRef]
44. Afify, A.M.; Sanz-Montero, M.E.; Calvo, J.P.; Wanas, H.A. Diagenetic origin of ironstone crusts in the Lower Cenomanian Bahariya Formation, Bahariya Depression, Western Desert, Egypt. *J. Afr. Earth Sci.* **2015**, *101*, 333–349. [CrossRef]
45. Afify, A.M.; Sanz-Montero, M.E.; Calvo, J.P. Ironstone deposits hosted in Eocene carbonates from Bahariya (Egypt)—New perspective on cherty ironstone occurrences. *Sediment. Geol.* **2015**, *329*, 81–97. [CrossRef]
46. Afify, A.M.; Sanz-Montero, M.E.; Calvo, J.P. Differentiation of ironstone types by using rare earth elements and yttrium geochemistry—A case study from the Bahariya region, Egypt. *Ore Geol. Rev.* **2018**, *96*, 247–261. [CrossRef]
47. Salem, S.M. ASD field hyperspectral measurements for discrimination of the ferruginous rocks and the iron ore types at El Gedida-Ghorabi area, Bahariya Oasis, Western Desert, Egypt. *Arab. J. Geosci.* **2017**, *10*, 166. [CrossRef]
48. Afify, A.M.; Serra-Kiel, J.; Sanz-Montero, M.E.; Calvo, J.P.; Sallam, E.S. Nummulite biostratigraphy of the Eocene succession in the Bahariya Depression, Egypt: Implications for timing of iron mineralization. *J. Afr. Earth Sci.* **2016**, *120*, 44–55. [CrossRef]
49. Baioumy, H.M.; Khedr, M.Z.; Ahmed, A.H. Mineralogy, geochemistry and origin of Mn in the high-Mn iron ores, Bahariya Oasis, Egypt. *Ore Geol. Rev.* **2013**, *53*, 63–76. [CrossRef]
50. El Aref, M.; El Sharkawi, M.; Khalil, M. Geology and genesis of the stratabound and Stratiform Cretaceous–Eocene iron ore deposits of the Bahariya region, Western Desert, Egypt. In Proceedings of the GAW 4th International Conference, Cairo, Egypt, 21–25 February 1998; Cairo University: Cairo, Egypt, 1999; pp. 450–475.
51. El Aref, M.M.; Mesaed, A.A.; Khalil, M.A.; Salama, W.S. Stratigraphic setting, facies analyses and depositional environments of the Eocene ironstones of Gabal Ghorabi mine area, El Bahariya Depression, Western Desert, Egypt. *United Arab. Repub. J. Geol.* **2006**, *50*, 29.
52. Williamson, D.A. Unified Rock Classification System1. *Environ. Eng. Geosci.* **1984**, *xxi*, 345–354. [CrossRef]
53. *BS EN 12407:2007*; Natural Stone Test Methods-Petrographic Examination. British Standards Institution: London, UK, 2007.
54. *ASTM C119*; Standard Terminology Relating to Dimension Stone. ASTM International: West Conshohocken, PA, USA, 2014.
55. *ASTM C97*; Standard Test Methods for Absorption and Bulk Specific Gravity of Dimension Stone. ASTM International: West Conshohocken, PA, USA, 2015.
56. Brunauer, S.; Emmett, P.H.; Teller, E. Adsorption of Gases in Multimolecular Layers. *J. Am. Chem. Soc.* **1938**, *60*, 309–319. [CrossRef]
57. *BS 812-110*; Methods for Determination of Aggregate Crushing Value (ACV). British Standards Institution: London, UK, 1990; Volume 110.
58. *BS 812-112*; Method for Determination of Aggregate Impact Value (AIV). British Standards Institution: London, UK, 1990.
59. *ASTM E1621*; Standard Guide for Elemental Analysis by Wavelength Dispersive X-ray Fluorescence Spectrometry. ASTM International: West Conshohocken, PA, USA, 2013.
60. *ASTM D7348*; Standard Test Methods for Loss on Ignition (LOI) of Solid Combustion Residues. ASTM International: West Conshohocken, PA, USA, 2013.
61. Masoud, M.A. Effect of Geochemical Composition of Some Egyptian Serpentinites on Its Properties as a Radiation Shielding Concrete. Master's Thesis, Beni-Suef University, Beni Suef, Egypt, 2020.
62. Sosa, C.S.; Flaska, M.; Pozzi, S.A. Comparison of analog and digital pulse-shape-discrimination systems. *Nucl. Instrum. Methods Phys. Res. Sect. A Accel. Spectrometers Detect. Assoc. Equip.* **2016**, *826*, 72–79. [CrossRef]
63. Ruch, M.L.; Flaska, M.; Pozzi, S.A. Pulse shape discrimination performance of stilbene coupled to low-noise silicon photomultipliers. *Nucl. Instrum. Methods Phys. Res. Sect. A Accel. Spectrometers Detect. Assoc. Equip.* **2015**, *793*, 1–5. [CrossRef]
64. El-Khayatt, A.M. NXcom—A program for calculating attenuation coefficients of fast neutrons and gamma-rays. *Ann. Nucl. Energy* **2011**, *38*, 128–132. [CrossRef]
65. Kaplan, M.F. *Concrete Radiation Shielding*; Longman Scientific & Technical: London, UK, 1989; p. 476.
66. Dabous, A.A. Uranium isotopic evidence for the origin of the Bahariya iron deposits, Egypt. *Ore Geol. Rev.* **2002**, *19*, 165–186. [CrossRef]
67. Çelen, Y.; Evcin, A.; Akkurt, I.; Bezir, N.; Günoğlu, K.; Kutu, N. Evaluation of boron waste and barite against radiation. *Int. J. Environ. Sci. Technol.* **2019**, *16*, 5267–5274. [CrossRef]
68. Masoud, M.A.; Kansouh, W.A.; Shahien, M.G.; Sakr, K.; Rashad, A.M.; Zayed, A.M. An experimental investigation on the effects of barite/hematite on the radiation shielding properties of serpentine concretes. *Prog. Nucl. Energy* **2020**, *120*, 103220. [CrossRef]

69. Jaeger, R.G.; Blizard, E.P.; Chilton, A.B.; Grotenhuis, M.; Hönig, A.; Jaeger, T.A.; Eisenlohr, H.H. *Engineering Compendium on Radiation Shielding*; Volume Shielding Fundamentals and Methods; Springer: New York, NY, USA, 1975.
70. Zayed, A.M.; Masoud, M.A.; Shahien, M.G.; Gökçe, H.S.; Sakr, K.; Kansouh, W.A.; El-Khayatt, A.M. Physical, mechanical, and radiation attenuation properties of serpentine concrete containing boric acid. *Constr. Build. Mater.* **2021**, *272*, 121641. [CrossRef]
71. Masoud, M.A.; El-Khayatt, A.M.; Kansouh, W.A.; Sakr, K.; Shahien, M.G.; Zayed, A.M. Insights into the effect of the mineralogical composition of serpentine aggregates on the radiation attenuation properties of their concretes. *Constr. Build. Mater.* **2020**, *263*, 120141. [CrossRef]